



HAL
open science

Roughness characteristic length scales of micro-machined surfaces: A multi-scale modelling

Maxence Bigerelle, Alexis Gautier, Alain Iost

► **To cite this version:**

Maxence Bigerelle, Alexis Gautier, Alain Iost. Roughness characteristic length scales of micro-machined surfaces: A multi-scale modelling. *Sensors and Actuators B: Chemical*, 2007, Functional Materials for Micro and Nanosystems EMRS, Containing Selected papers from the European Materials research Society (E-MRS 2006) Symposium G:, 126 (1), pp.126-137. 10.1016/j.snb.2006.11.006 . hal-01326529

HAL Id: hal-01326529

<https://hal.science/hal-01326529>

Submitted on 10 Mar 2017

HAL is a multi-disciplinary open access archive for the deposit and dissemination of scientific research documents, whether they are published or not. The documents may come from teaching and research institutions in France or abroad, or from public or private research centers.

L'archive ouverte pluridisciplinaire **HAL**, est destinée au dépôt et à la diffusion de documents scientifiques de niveau recherche, publiés ou non, émanant des établissements d'enseignement et de recherche français ou étrangers, des laboratoires publics ou privés.

Roughness characteristic length scales of micro-machined surfaces: A multi-scale modelling

Maxence Bigerelle^{a,*}, Alexis Gautier^a, Alain Iost^b

^a *Laboratoire Roberval, CNRS FRE 2833, UTC Centre de Royallieu, BP 2059 Compiègne, France*

^b *Equipe Caractérisation et Propriétés des Périsurfaces, LMPGM, CNRS UMR 8517, ENSAM, 8, Boulevard Louis XIV, 59046 LILLE CEDEX, France*

Abstract

The MEMS structure integrity, their dynamic properties as well as their electrostatic characteristics, strongly depend on the achieved surfaces roughness produced by the micromachining process. It is therefore, not surprising that numerous works are devoted to propose relations between roughness and physical or mechanical properties in this field. Yet the issue is full of complexities since roughness parameters depend on the method used for their evaluation. This article introduces a new approach of the roughness characterization, based on the scaling analysis. Experimental results obtained on micro machined surfaces show that the range roughness amplitude depends on the scan length and that roughness amplitude follows three stages. The stage I is due to a smoothing effect of the surface induced by the tip radius of the profilometer, stage II presents a piecewise power-law roughness distribution until a critical length that characterises the fractal behaviour of the surface, and stage III is characterised by extreme values statistics. The fractal parameter, the extreme values estimators and the crossover between stages II and III are shown to be related to the micromachining process. As a result, an original probabilistic model based on the Generalized Lambda Distribution (GLD) is proposed to estimate the multi-scale roughness in the stage III. Finally, thanks to a Bootstrap protocol coupled with a Monte-Carlo simulation, the maximal roughness amplitude probability density function is estimated at a scale higher than the scanning length.

Keywords: Roughness; High precision machining; dimensional tolerance; Extreme values; Fractal; Topography modelling

1. Introduction

In the past three decades, important progresses have been preceded in the field of high precision machining techniques. Some of them as ions beams, electrons or laser are usually used in the microelectronic industry. Surface topography obtained by high precision machining are of major interest. In the case of glass etching, the RMS surface roughness is as less than 2 nm [1] and plays a major role for silicon bulk micromachining [2]. Electrical resistivity and HF permeability are influenced by the surface topography even for low roughness [3]. For example, to minimize the air gap in linear actuators, the microactuator's surface needs a very low roughness [4] that prevents magnetic field interference [5]. Surface quality is of major interest for nano-displacement sensors considered as mirror reflection [6] based

on optical properties (like Fabry-Perot one) that integrates an emerging field of the MEMS of the digital micro mirror device [7]. Classically, polishing techniques allow obtaining very high quality surface in optical domain (mirror finishing) with less than 1 nm average roughness. Surface roughness plays a profound influence in the case of stiction/adhesion, friction or wear and consequently on the micro/nanoelectromechanical systems reliability [8]. The roughness friction coefficient [9] dependence leads adapting process to diminish the roughness [10,11], particularly for increasing micro motors service lifetime [12]. High precision turning (HPT) is now used when very good dimensional or geometrical tolerances (lower than 1 μm) and high surface quality (roughness less than 50 nm) are required to reach the specifications imposed by mechanical or optical industries for revolution parts [13,14]. The main objective of this superfinishing process is to avoid successive operations and thus, to manufacture a component using only a single machine. All the machine elements taking part in the kinematics are of great importance, but the tool, which is the last link in direct con-

* Corresponding author.

E-mail address: maxence.bigerelle@utc.fr (M. Bigerelle).

tact with the part, “prints” its mark on the surface and must be chosen with great care. For ductile materials as aluminium alloys, poly-crystal diamond (PCD) tools are used, but unfortunately average surface roughness cannot decrease down to less than 20 nm. As a result, single-crystal diamond (SCD) tools are used when less than 10 nm roughness amplitude must be reached [15,16]. Moreover, to characterise the low roughness of such surfaces and their structural integrity, high resolution measurement techniques have to be used. As it was described, MEMS structure integrity, dynamic properties as well as electrostatic characteristics, strongly depend on the achieved surfaces roughness produced by the micromachining process. Yet the issue is full of complexities since roughness parameters depend on the method used for their evaluation. This paper outlines a new approach to roughness characterization, based on scaling analysis. A serious difficulty is that all the micro machined surface topography cannot be recorded because the limits of the maximal scanning length: AFM areas rarely exceed $100\ \mu\text{m} \times 100\ \mu\text{m}$, and confocal or interferometric microscopy scanning is imposed by lens magnitude and camera resolution often limited to 1024×1024 pixels that does not allow to both having high definition and high scanning area. To characterise roughness surfaces, the Peak to Valley parameter [17,18] that represents the range of the roughness amplitude (called R_t or PV) is of major interest in the case of dimensional tolerance characterisation for MEMS. However, this parameter depends on the evaluation length [19,20] and as the scanning area is often lower than the part area, the R_t parameter of the part cannot be evaluated on the whole surface. As a consequence, a multi-scale modelling has to be constructing to extrapolate data from the sampling length to the whole sample. The original method we proposed allows both predicting maximal range amplitude versus the length of the part and giving confidence intervals of the predicted values. Without lack of generality, we shall apply our methodology on the surface topography of a pure aluminium part machined by high precision turning process with a single-crystal diamond tool. In a first part, the mating process is precised and the roughness measurements protocol is described. After surface topography multi-scale analyses, a prediction model is proposed and validates at different scales.

2. High precision turning process

Obtaining good surface quality requires both the lack of vibrations and thermal drift, and tool straight trajectories that impose the respect of strict conditions when designing a high precision machine. It is also imperative to control the machine environment. The centring of the part is of main importance to avoid an imbalance of the spindle and thus, a false round [21]. Moreover, to obtain high dimensions accuracy, the adjustment of the tool compared to the spindle axis must be carried out with a micrometer precision. The high precision machine used in this study is a prototype lathe positioned in an air-conditioned room [22]. The two slides are fixed on a massive granite block (1.5 tonnes), itself resting on four self-levelling pneumatic isolators. The slide-ways are guided by hydrostatic-bearings, offering low friction and high stiffness and damping.

The straightness of both slides is better than $0.3\ \mu\text{m}$ over a displacement of 100 mm. Recently, linear motors (ILD-EtelTM) have replaced both the classic brushless motors and the ball screws. As a result, the dynamic stiffness of the transmission is increased while the reduced number of machine elements limits parasitic forces. The command transfer function is changed, because the mass in movement is reduced. Otherwise, displacements are measured by two 4 nm resolution optical encoders (LIP 101-HeidenhainTM) controlled by an accurate Computer Numerical Control system (CNC) with a powerful numerical card (PMAC-DeltatauTM). Owing to the speed of computing and integrated functions, the rise time of the close loop is very short and complex forms can be machined with high precision. A magnetic-bearing spindle (with active control) is located on the z-axis slide-way. A magnetic plate is used; if the material is nonmagnetic, the specimen is stuck on a steel support or held in a chuck. As it was previously mentioned, single-crystal diamond is a very accurate cutting tool, because its great rigidity, its very high hardness and its good thermal conductivity. Moreover, the quality of its edge of cut, make it possible to form very low thickness chips of some micrometers without cold-working the material surface. The interest of single-crystal tool, compared to polycrystalline one, is that its single edge can have a very low waviness, and that one can easily choose the most favourable crystallographic plans $\{1\ 1\ 0\}$ in term of wear [23,24]. On the contrary, the polycrystalline cutting edge consists of multiple small grains, stuck one to another, with a quasi-random orientation that induces higher surface roughness on machined surfaces. However, tool must be chosen with great care in relation to the nature of the machining material: the chemical interaction between diamond tool and carbide-forming elements present in the material restricts the number of machinable materials to light alloys (aluminium and copper) and also to non-metal materials as germanium, silicon and polymers. On the other hand, steels, titanium alloys and nickel cannot be machined by diamond tool, because the edge tool would be drastically destroyed by the chemical wear. A lubrication air pressed system with a fine mist of lubricant operates during machining. The objective when a ductile material as aluminium is machined with a SCD tool is to evacuate the chip to prevent surface damage. The work piece is an aluminium disk with a 35 mm diameter and a 6 mm thickness. Samples were stuck on a steel support fixed on the magnetic plate of the spindle. The machining parameters were fixed as follows: a 1250 rpm spindle speed (cutting speed of 165 m/min), a $4.8\ \mu\text{m}/\text{rev}$ advance speed and a $10\ \mu\text{m}$ finishing depth of cut for a SCD tool with a 5° rake angle and a 1.5 mm nose radius [25].

3. Roughness analyses

3.1. Roughness measurements

Nine profiles are recorded perpendicularly to the grooves over a $0.1\ \mu\text{m}$ sampling length, a 4.5 mm scanning length (45,000 amplitude roughness data per profile) and a $100\ \mu\text{m}/\text{s}$ scanning speed. The surface recorder is a high precision tactile profilometer 3D KLA TENCORTM P10 firstly developed to measure MEMS surface in electronic devices industry. The experimen-

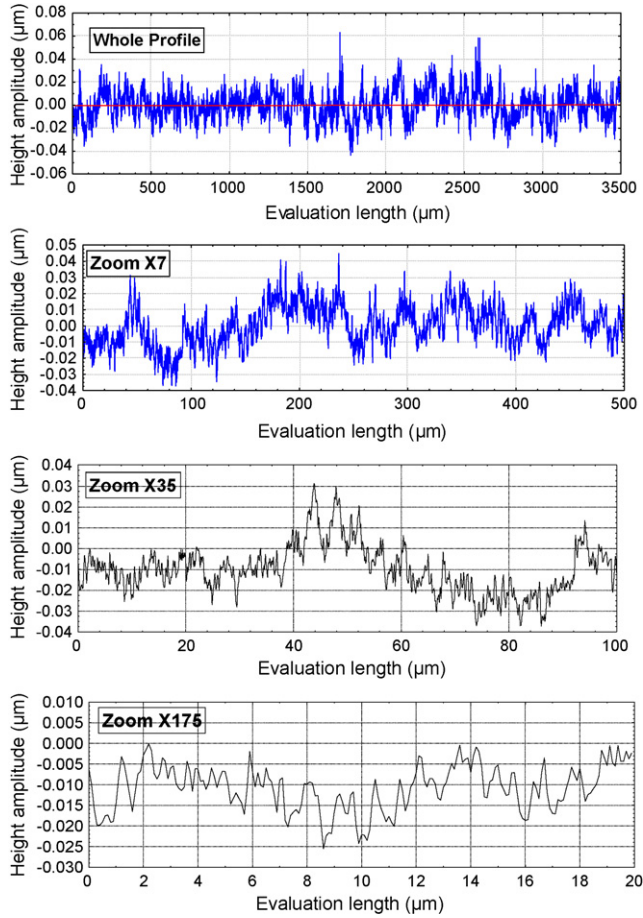


Fig. 1. Recorded profile of an aluminium surface toolled with HPT with three spatial zoom (X7, X35, X175) located at the origin of the whole profile.

tal conditions are: $2\ \mu\text{m}$ for the stylus radius and $5\ \text{mg}$ for the applied load. The instrument has a vertical resolution better than $10\ \text{nm}$, and a lateral resolution of $50\ \text{nm}$ on the x axis and $1\ \mu\text{m}$ on the y axis. Each profile was fitted by a least mean square third degree polynomial to remove the form and keep only waves and roughness. Fig. 1 represents a profile recorded on the toolled surfaces with three spatial zoom (X7, X35, X175) located at origin of the profile plot.

3.2. Multi-scale roughness analyses

The functionality of micromachined surfaces is often influenced by their topography at a given scale. The arithmetic average height (R_a) and the total amplitude (R_t) also called the “Peak to Valley” are very often used to characterize the surface roughness irregularities but, in most studies, the effect of the evaluation length is not taken into account. This is all the more unfortunate since these parameters depend on the observation scale [20,26]. Such a kind of dependence is integrated in the fractal concept, which basis is to find invariant scale parameters. Since its introduction by Mandelbrot [27], several mathematical methods have been established to measure this fractal dimension and to characterise the surface roughness independently of the observation scale [28].

3.2.1. Basic concept

After this preliminary step, the objective of the data treatment was to calculate the roughness amplitude parameter $R_t = Y_{\max} - Y_{\min}$ as a function of the evaluation length. As far as R_t is concerned, it can be expected that the probability to record high peaks (i.e., high value of Y_{\max}) or deep valleys (i.e., small value of Y_{\min}) is all the more important as far as the evaluation length l increases. It is worth noting that the evaluation length l is present in the original definition of the arithmetic average roughness parameter: $R_a = \frac{1}{l} \int_0^l |y(x)| dx$, and consequently it can be expected that the evaluation length may also affects its value. For the total evaluation length of our investigated surfaces, the value $R_a = 9.7\ \text{nm}$ was found. Recall that, for each 2D profile i ($1 \leq i \leq 9$), 45,000 points are recorded with an interval Δx between two consecutive points equals to $\Delta x = 0.2\ \mu\text{m}$. In our algorithm, the values of Y_{\max} and Y_{\min} are computed to calculate a local value of R_t noticed $R_t(x, l) = Y_{\max}(x, l) - Y_{\min}(x, l)$ for a given evaluation length l beginning at the x position of the evaluation length (x and l varying from 0 to the value of a trace length i.e., $4.5\ \text{mm}$) on the residual profile i . Then, the evaluation window of length l is shifted by a quantity x ($x \in [\Delta x, L - \Delta x]$) to estimate a new local value $Y_{\max}^1(x, l+x)$, $Y_{\min}^1(x, l+x)$ and $R_t^1(x, l+x)$ noted, respectively $Y_{\max}^x(l)$, $Y_{\min}^x(l)$ and $R_t^x(l)$. This operation is repeated until the end of the residual profile i is reached. Then all the local values $Y_{\max}^x(l)$, $Y_{\min}^x(l)$ and $R_t^x(l)$ are averaged for all x values to determine ‘averaged l values’ $Y_{\max}(l)$, $Y_{\min}(l)$ and $R_t(l)$ corresponding to an observation scale l for the residual profile i . Fig. 2 represents the multiscale roughness values of $Y_{\max}(l)$, $Y_{\min}(l)$ and $R_t(l)$ at different observation scales l for the nine recorded profiles. The following primary remarks can be stated from these graphics:

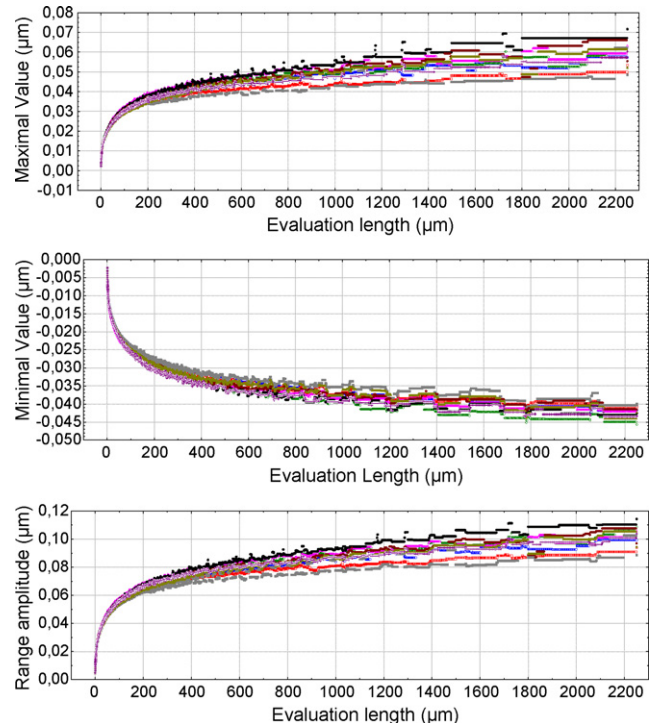


Fig. 2. $Y_{\max}(l)$, $Y_{\min}(l)$ and $R_t(l)$ multi-scale roughness values at different observation scales l for nine recorded aluminium surface profiles toolled with HPT.

- Apparently, the amplitude of the three roughness parameters $Y_{\max}(l)$, $-Y_{\min}(l)$ and $R_t(l)$ increases logarithmically with the evaluation length l . This scale effect is due to the fact the amplitude of peaks and valleys decreases with the scale (see Fig. 1).
- Dispersion of the data increases with the evaluation length l . As it can be observed, curves are more and more scattered as the evaluation length increases. This second scale effect constitutes the basic concept of this paper and will be discussed later. However, it clearly means that the accuracy to predict a maximal or minimal values depends drastically of the evaluation length and will be less and less precise as the evaluation length increases.
- It can be observed that the value $Y_{\max}(l) > -Y_{\min}(l)$ and the difference increase with the evaluation length l . $Y_{\max}(0.2 \mu\text{m}) = 2.3 \text{ nm}$ increases to $Y_{\max}(4500 \mu\text{m}) = 58 \text{ nm}$ and $Y_{\min}(0.2 \mu\text{m}) = 2.3 \text{ nm}$ increases to $Y_{\min}(4500 \mu\text{m}) = 42 \text{ nm}$. To explain this result, some precisions must be tackled about the algorithmic computation of the reference line from which profile amplitude is estimated (origin of amplitude from which deviation is computed as shown on Fig. 1). For each recorded profile $R(x)$, the statistical treatment firstly consists in fitting by the least square method a third order polynomial $P(x)$ curve to the raw measured profile to remove the eventual form and waviness. Multi-scale roughness parameters are computed on this residual profile $Y(x) = R(x) - P(x)$. A property of the least square method involves that the average on x of $Y(x)$ is null. As a result, if maximal values appear to be greater than the minimal one, that clearly means that the probability density functions of the roughness amplitude is skewed denoting that peaks are higher than valleys. This skewness can be explained by two morphological properties of the surfaces. Firstly, it is well known than tooled surfaces obtained by the turning process present a morphological structure that looks like a U-shaped periodical profile (half-circle function), which period is specified by the feed rate. Consequently, the distance between the maximal height amplitude and the reference line is higher than the distance from minimal valley to the reference line. Secondly, plasticity and abrasion resulting from the interaction between tool and aluminum induced piled-up region concentrated on profile peaks, leading to an increase of the maximal peak amplitude.

3.2.2. Multi-scale analysis

For each experimental profile under consideration, the averaged local values $R_t(l)$ of the nine related residual profiles are all averaged to obtain a final mean \bar{R}_t value at an evaluation length l . Fig. 3 shows the variation of $\bar{R}_t(l)$ versus the evaluation length in log-log coordinates. From this graphics, three different stages emerge: two linear and a logarithmic one. By means of appropriate statistical techniques proposed earlier by the authors to describe the different stages in fatigue crack growth propagation [29], it can be stated that these three stages limits are:

- $l < 4 \mu\text{m}$ (log-log linear stage),
- $l \in [4 \mu\text{m}, 60 \mu\text{m}]$ (log-log linear stage) and
- $l > 60 \mu\text{m}$ (log-log logarithmic stage).

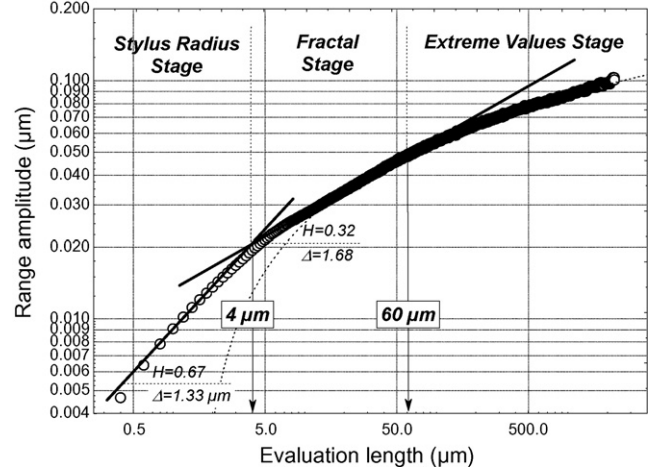


Fig. 3. $R_t(l)$ multi-scale mean roughness values at different observation scales l obtained by averaging the nine recorded aluminium surface profiles tooled with HPT shown in Fig. 2.

The stage transition can play a dominant role on MEMS response such the pull-in voltage in micro switches [30]. For lack of simplicity, the stage II analysis will be firstly introduced.

3.2.3. Stage II: the fractal stage

By analyzing Fig. 3, $R_t(l)$ presents a linear aspect in the log-log representation in the range $l \in [4 \mu\text{m}, 60 \mu\text{m}]$ with a slope equals to 0.32. This clearly means that the scale relation $R_t(l) \propto l^{0.32}$ holds. To explain this relation, the determination of the fractal dimension by “Oscillation Method” from Dubuc et al. [20,26] must be introduced. The τ -oscillation of the function f in x is defined as:

$$f : [a, b] \rightarrow \mathbb{R} \quad \text{OSC}_\tau(f, x) = \left| \max_{|x-t| < \tau} (f(t)) - \min_{|x-t| < \tau} (f(t)) \right|, \quad (1)$$

by taking the average of $\text{OSC}_\tau(f, x)$ over the interval $[a, b]$, one obtains:

$$\text{VAR}_\tau(f, a, b) = \frac{1}{b-a} \int_a^b \text{OSC}_\tau(f, x) dx \quad (2)$$

then the fractal dimension can be written as:

$$\Delta(f, a, b) = \lim_{\tau \rightarrow 0} \left(2 - \frac{\log \text{VAR}_\tau(f, a, b)}{\log \tau} \right) \quad (3)$$

If the function f is given by the experimental profile f_e , then:

$$R_t^x(l) = \text{OSC}_l(f_e, 0, l) \quad (4)$$

and finally by introducing Eq. (4) in Eq. (2) the following result is obtained:

$$R_t(l) = \text{VAR}_l(f_e, 0, l) \quad (5)$$

From Eq. (3), the fractal dimension $\Delta(f_e, 0, L)$ of the f_e profile is equals to 2 minus the slope called the Hölder exponent, therefore, the fractal dimension in the stage two is: $\Delta(f_e, 0, 4500 \mu\text{m}) = 1.68$. It is reported that tool machined surfaces possess fractal aspect [31–37] and additionally in nanomachining process on aluminium surfaces [38] that is quit

similar to the machining process discussed in this paper. In this pure fractal stage, it becomes then possible to predict the values of the maximal roughness amplitude $R_t(l)$ versus the evaluation length and their associated confidence intervals thanks to conventional statistical tools used under the Gauss Markov hypothesis in the linear regression modelling. However, the mathematical formalism of stages (I) and (III) is still not justified in the bibliography and then the predictions of the maximal roughness amplitude at these given scales cannot be predicted. Lets now analyse physically the meaning of the stage I and III. The stage I presents a linear relation in a log–log plot with slope equal to 0.67 meaning that the fractal dimension is equal to 1.33. Compared to the stage II, the fractal dimension decreases meaning that the profiles appear smoother when $l < 4 \mu\text{m}$. This involves that a new process appears that diminishes the fractal dimension of the profiles for a small scale length. At the larger scale ($l > 60 \mu\text{m}$, stage III), the linear relation does not hold meaning that the fractal concept does not applied. As a consequence, the fractal concept of tooled surface cannot be extended to large spatial scale. We postulate that the transition stage II–stage III is linked to a change of the fractal properties of the profile. It is reported in the bibliography that fractal properties of profiles may be determined by autocorrelation functions [39,40]. For this reason the average autocorrelation function of all profiles is plotted in Fig. 4. As it can be observed, the autocorrelation decreases and presenting an oscillation until reaching a null value (in spatial average) for $l > 60 \mu\text{m}$. Thanks to a spectral analysis (Fig. 5), the period of this oscillation is equal to $4.6 \mu\text{m}$, a value closed to the advance speed ($4.8 \mu\text{m}/\text{rev}$) of the turning process. However, after the stage II ($l > 60 \mu\text{m}$), auto-correlation values is null meaning that no “memory” of the profile occurs when two measured amplitude height values are distant of more than $60 \mu\text{m}$. As a consequence, pass over this critical length, profiles may be analysed as a pure random process with appropriate mathematical tools. Stage III is of major interest because it assumes the dimensional tolerance of the MEMS. Although often mentioned in the bibliography, the mathematical and physical backgrounds of this stage is never justified.

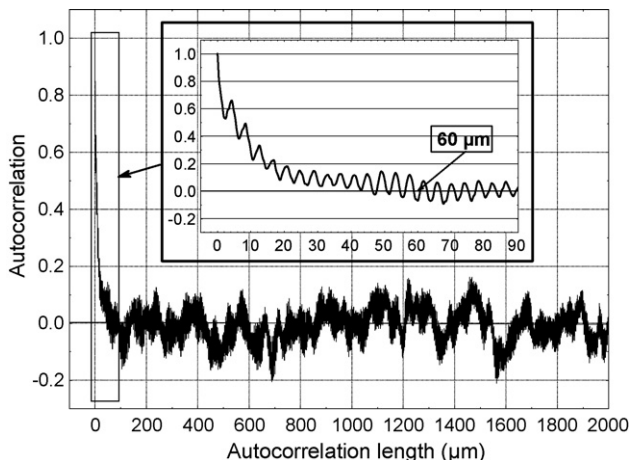


Fig. 4. Average autocorrelation functions for the nine recorded profiles of an aluminium surface tooled with HPT.

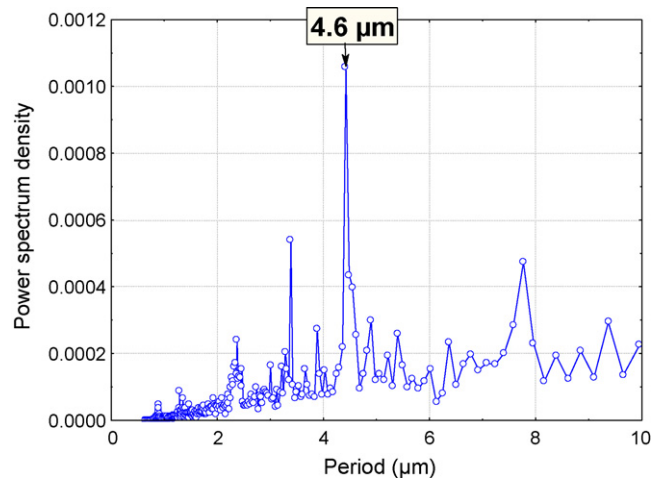


Fig. 5. Average power spectrum of the nine aluminium surface recorded profiles tooled with HPT.

3.2.4. Stage I: the radius stylus tip stage

As seen above, profiles appear smoother for $l < 4 \mu\text{m}$, a value that corresponds exactly to the diameter of the profilometer tip. The tactile recording involves a certain amount of smoothing or degradation of the true surface data. The stylus curvature radius produces a smoothing effect of the recorded profile since the stylus cannot record any information at all from crevices that are narrower than the stylus width. However, as the smoothing effect is a highly non-linear convolution of the profile, it becomes very difficult to estimate its effect on the original data. Consequently, it is of major interest to determine the scale at which the smoothing effect plays a part in the roughness parameters calculation. The stylus size effect is greatly discussed in the bibliography for mechanical profilometers [41–45] and AFM topography [46–48], however, no universal analytical expression characterises the smoothing effect whatever the surface topography. For this reason, an algorithm that simulates the stylus effect on surface integration was written and applied on a simulated fractal profile, free of the stylus integration effect, that looks like our experimental function (see appendix, simulation of turning surface). Fig. 6 represents surface profiles simulated by fractal functions described in Annexe. As it could be observed, the profiles obtained are very relevant to model the high finish surfaces and can be used for multi-scale function analysis. Stylus scanning effects were simulated with $1\text{--}5 \mu\text{m}$ curvature radii. Fig. 7 shows the good agreement between profiles simulated with a $2 \mu\text{m}$ profilometer radius and the experimental one (Fig. 1). Measuring the range amplitude roughness on the six different curvature radii simulated profiles, it can be observed on Fig. 8 that the crossover Stage I–Stage II appears towards $4 \mu\text{m}$ for a tip diameter of $4 \mu\text{m}$ and increases with the stylus tip diameter. The simulation confirms the fact that this stage is related to the smoothing effect of the surface implicated by the tactile covering (the same effect occurs in AFM measurements [48]).

3.2.5. Stage III: the extreme values stage

As noticed, the plot of R_t versus l in a log log plot (Fig. 3) presents a logarithmic stage (in a log–log coordinate) for

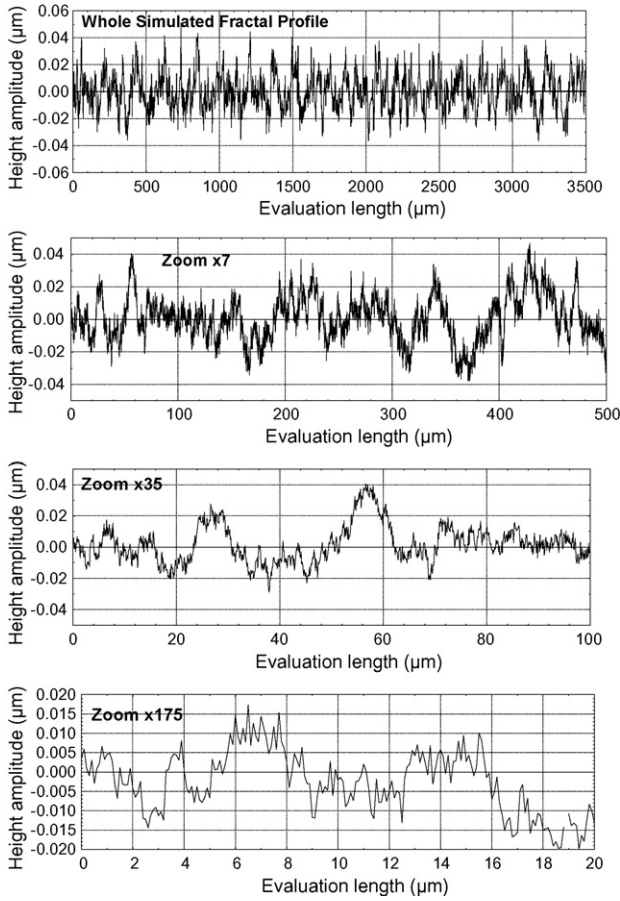


Fig. 6. Simulated profile of surface tooling with HPT as shown in Fig. 1 with three spatial zoom (X7, X35, X175) located at the origin of the whole profile.

$l > 60 \mu\text{m}$ that we have presented as a pure stochastic process. To the authors' knowledge, no modelling was proposed in the bibliography to predict the maximal range amplitude after this threshold. To account for, we postulate that the surface becomes stationary in a statistical sense (ergodicity) after the fractal stage, meaning that the mean amplitude of the surface stays constant. However, by including the sampling effect, the fluctuation occurs and the magnitude of the extremes values increases with the number of sampling points. The most successful method of safety or reliability was found in the application of the statistical extreme value analysis using the Gumbel distribution [49]. Because some limitations (no interval confidence intervals for extreme value predictions, properties of the parent distribution are imposed), an alternative method-

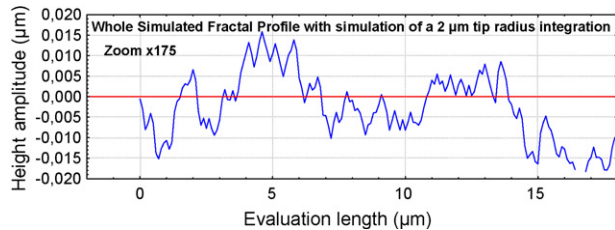


Fig. 7. Fig. 6 simulation of stylus integration ($2 \mu\text{m}$ radius) with a X175 spatial zoom.

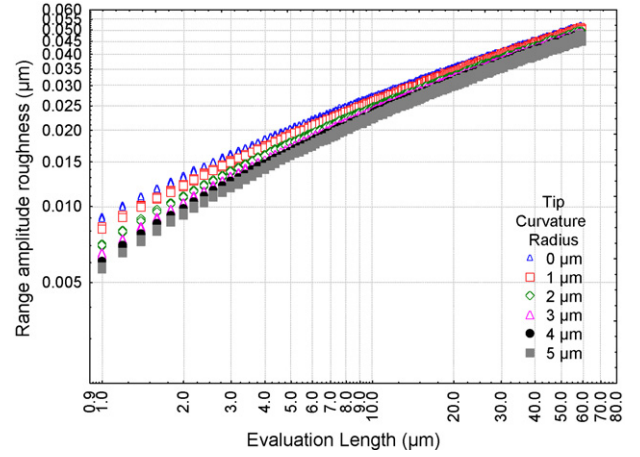


Fig. 8. $R_t(l)$ multi-scale roughness values computed at different observation scales l from simulated profile with stylus integration processed for different tactile profilometer stylus radii.

ology to the Gumbel distribution shall be proposed in this paper.

4. The prediction of the extreme amplitude roughness

The method we shall develop here consists to predict the extreme values of the surface roughness parameters $Y_{\max}(l)$, $Y_{\min}(l)$ and $R_t(l)$, and their associated uncertainties, by measurement at a given scale l . The resolution of this problematic is of major interest in high finish surface control because surfaces topography are rarely recorded in totality (high time consuming, limitation of scanning length of profilometers. . .). The methodology we proposed as an alternative methodology to the Gumbel distribution is based on the combination of two statistical methods: the Generalized Lambda Distribution (GLD) [50] and the Monte-Carlo method. Contrary to the Gumbel approach that requires a parent distribution of exponential type to be applied, both the GLD and the Monte-Carlo methods present the main advantage to avoid making any assumption about the underlying distribution. Moreover, the GLDs have been shown to fit well many of the most important distributions including exponential type ones. The normal (Gaussian), exponential and Lognormal distributions belong to this type and are often observed in case of engineering surface data. It must be outlined that the goodness of fit by the GLD is particularly noticeable in the tail region of this kind of distributions; region of interest of this study since it corresponds to the extreme values of any distribution.

4.1. Modelling the maximal, minimal and range amplitude distribution

It will now supposed that the roughness measurement is processed on a evaluation length that corresponds to the end of the fractal stage i.e., $l = 60 \mu\text{m}$. Fig. 9 represents the histogram of all $Y_{\max}^x(60 \mu\text{m})$, $Y_{\min}^x(60 \mu\text{m})$ and $R_t^x(60 \mu\text{m})$ local values. Then the first step consists in modelling these histograms thanks to the use of the Generalized Lambda Distribution. The GLD family is specified in terms of its percentile function (called also the

Empirical distributions of minimal, maximal and range roughness amplitude for an evaluation length of 60 μm

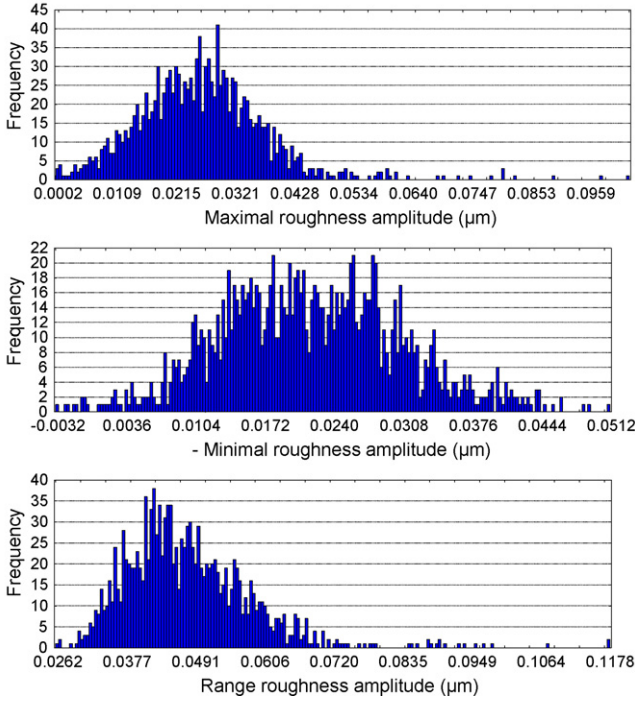


Fig. 9. Minimal $Y_{\min}(l)$, maximal $Y_{\max}(l)$, and range roughness amplitude $R_l(l)$ empirical distributions at $l = 60 \mu\text{m}$ evaluation scale.

inverse distribution function) with four parameters (λ_1 , λ_3 , λ_3 and λ_4):

$$Q_X(y; \lambda_1, \lambda_2, \lambda_3, \lambda_4) = \frac{\lambda_1 + (y^{\lambda_3} - (1 - y)^{\lambda_4})}{\lambda_2} \quad (6)$$

λ_1 and λ_2 are respectively, the location and the scale parameters, while λ_3 and λ_4 determine respectively, the skewness and the kurtosis of the GLD. The probability density function $f_X(x)$ can then be easily expressed from the percentile function of the GLD:

$$f_X(x) = \frac{\lambda_2}{(\lambda_3 y^{\lambda_3 - 1} + \lambda_4 (1 - y)^{\lambda_4 - 1})} \quad (7)$$

The main problem is to estimate the parameters $\lambda_1, \lambda_2, \lambda_3$ and λ_4 in order to have the best fitting of the GLD with the experimental frequency distribution (of extreme roughness values in this study). In a first time empirical moment are calculated from n experimental data x_i :

$$\hat{\alpha}_1 = \frac{\sum_{i=1}^n x_i}{n} \quad (8)$$

$$\hat{\alpha}_2 = \frac{\sum_{i=1}^n (x_i - \hat{\alpha}_1)^2}{n} \quad (9)$$

$$\hat{\alpha}_3 = \frac{\sum_{i=1}^n (x_i - \hat{\alpha}_1)^3}{n \hat{\alpha}_2^{3/2}} \quad (10)$$

$$\hat{\alpha}_4 = \frac{\sum_{i=1}^n (x_i - \hat{\alpha}_1)^4}{n \hat{\alpha}_2^2} \quad (11)$$

It is shown [50] that:

$$\alpha_1 = \lambda_1 + \frac{A}{\lambda_2} \quad (12)$$

$$\alpha_2 = \sigma^2 = \frac{B - A^2}{\lambda_2^2} \quad (13)$$

$$\alpha_3 = \frac{C - 3AB + 2A^3}{\lambda_2^3 \alpha_2^{3/2}} \quad (14)$$

$$\alpha_4 = \frac{D - 4AC + 6A^2B + 3A^4}{\lambda_2^4 \alpha_2^2} \quad (15)$$

with

$$A = \frac{1}{1 + \lambda_3} - \frac{1}{1 + \lambda_4}, \quad (16)$$

$$B = \frac{1}{1 + 2\lambda_3} + \frac{1}{1 + 2\lambda_4} - 2\beta(1 + \lambda_3, 1 + \lambda_4) \quad (17)$$

$$C = \frac{1}{1 + 3\lambda_3} + \frac{1}{1 + 3\lambda_4} - 3\beta(1 + 2\lambda_3, 1 + \lambda_4) + 3\beta(1 + \lambda_3, 1 + 2\lambda_4) \quad (18)$$

$$D = \frac{1}{1 + 4\lambda_3} + \frac{1}{1 + 4\lambda_4} - 4\beta(1 + 3\lambda_3, 1 + \lambda_4) + 6\beta(1 + 2\lambda_3, 1 + 2\lambda_4) - 4\beta(1 + \lambda_3, 1 + 3\lambda_4) \quad (19)$$

where

$$\beta(a, b) = \int_0^1 x^{a-1} (1-x)^{b-1} dx. \quad (20)$$

The moments of Y_{\max}^x (60 μm) and Y_{\min}^x (60 μm), estimated by Eqs. (8)–(11), are reported in Table 1. To calculate $\lambda_1, \lambda_2, \lambda_3$ and λ_4 , it is necessary to solve a four system of Eqs. (12)–(15) that are highly non linear. As Eqs. (18) and (19) depend only of λ_3 and λ_4 and as $\lambda_2^3 \sigma^3 = (B - A^2)^{3/2}$ and $\lambda_2^4 \sigma^4 = (B - A^2)^2$, the system is reduced to a two equations one with more stable numerical convergence (less numerous local extrema). The solution consists in finding λ_3 and λ_4 by a steepest gradient on the following functional:

$$\Psi'(\lambda_3, \lambda_4) = \sum_{i=3}^4 (\hat{\alpha}_i - \alpha_i)^2 \quad (21)$$

then λ_2 is calculated from Eq. (13) and finally λ_1 from Eq. (12). An algorithm was written in the Statistical Analyses System language (SASTM) to determine the GLD and its related probability density function from the experimental dataset. The numerical results of the minimization process obtained with our computer

Table 1
Moments of Y_{\max}^x (60 μm) and Y_{\min}^x (60 μm) distributions

	$\hat{\alpha}_1$	$\hat{\alpha}_2$	$\hat{\alpha}_3$	$\hat{\alpha}_4$
Y_{\max}^x (60 μm)	0.0214	0.0414	0.8930	0.3004
Y_{\min}^x (60 μm)	0.02572	0.0582	0.6519	0.2330

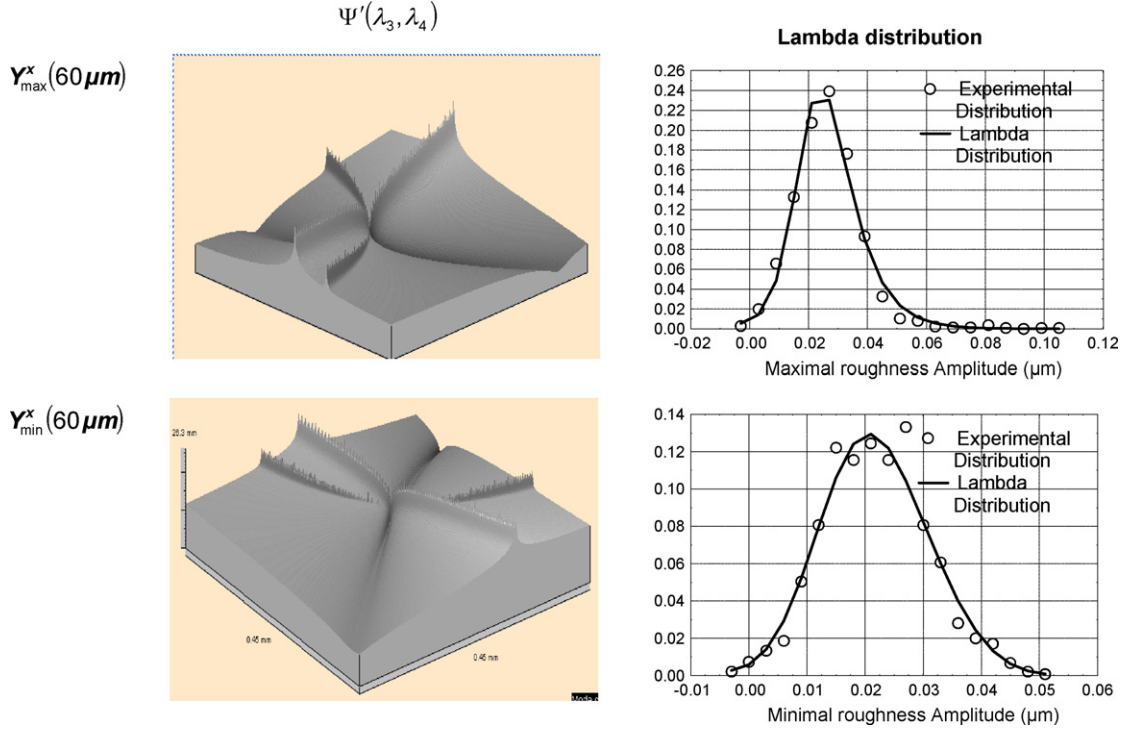


Fig. 10. 3D view of the values of the function $\Psi(\lambda_3, \lambda_4)$ for the lambda distribution associated with $Y_{\max}^x(60 \mu\text{m})$ and $Y_{\min}^x(60 \mu\text{m})$. On the right, $Y_{\max}^x(60 \mu\text{m})$ and $Y_{\min}^x(60 \mu\text{m})$ Lambda distribution obtained after minimization on $\Psi(\lambda_3, \lambda_4)$.

algorithm are illustrated in Fig. 10. These figures present a 3D view of the values of the function $\Psi(\lambda_3, \lambda_4)$ on which the gradient decreasing method was processed when $-2 < \lambda_3 < 1$ and $-2 < \lambda_4 < 2$ for the lambda distribution associated with $Y_{\max}^x(60 \mu\text{m})$ and $Y_{\min}^x(60 \mu\text{m})$. After minimization, the values of the four parameters for the both Lambda distributions that modeled $Y_{\max}^x(60 \mu\text{m})$ and $Y_{\min}^x(60 \mu\text{m})$; the related empirical distributions are shown in Table 2. Then the $Y_{\max}^x(60 \mu\text{m})$ and $Y_{\min}^x(60 \mu\text{m})$ Lambda distribution are plotted on Fig. 10. As it can be observed, the Lambda distributions fit very well the $Y_{\max}^x(60 \mu\text{m})$ and $Y_{\min}^x(60 \mu\text{m})$ empirical distributions. To appreciate the well accuracy of lambda distribution to model extreme data roughness, a Chi-2 criterion is computed. For both the data $Y_{\max}^x(60 \mu\text{m})$ and $Y_{\min}^x(60 \mu\text{m})$, the Chi-2 criterion does not reject the adequation between experimental and model data at the usual critical value $\alpha = 0.05$. This means that $Y_{\max}^x(60 \mu\text{m})$ and $Y_{\min}^x(60 \mu\text{m})$ both obey a Lambda distribution and this model can be used to predict some probabilistic features.

4.2. Multi-scale prediction of the distribution of the maximal, minimal and range amplitude roughness

At this stage, an analytical probability density function of $Y_{\max}^x(60 \mu\text{m})$ and $Y_{\min}^x(60 \mu\text{m})$ of the maximal and minimal local roughness amplitude is estimated at scale $l = 60 \mu\text{m}$. Supposing that the evaluation length is twice as large as the initial one (i.e., one wants to estimate $Y_{\max}^x(120 \mu\text{m})$), and that data are independent at this scale (as presently shown) then the maximal amplitude for two possible values of x and x' is equals to:

$$Y_{\max}(120 \mu\text{m}) = \max(Y_{\max}^x(60 \mu\text{m}), Y_{\max}^{x'}(60 \mu\text{m})) \quad (22)$$

In an algorithmic point of view, this means that one take randomly two values of $Y_{\max}^x(60 \mu\text{m})$ and the maximal value of this pair gives an estimation of the maximal roughness measured at a $120 \mu\text{m}$ evaluation length. By repeating a great number of times this procedure, the probability density function of $Y_{\max}^x(120 \mu\text{m})$ can be obtained. Extending this procedure, the values of $Y_{\max}^x(kl)$ are obtained by taking the maximal value from k values of $Y_{\max}^x(l)$. To simulate a possible value taken from $Y_{\max}^x(l)$, a random number that follows a Lambda distribution with parameters $(\lambda_1, \lambda_2, \lambda_3, \lambda_4)$ is generated using the following equation:

$$p(u) = \frac{\lambda_1 + (u^{\lambda_3} - (1 - u)^{\lambda_4})}{\lambda_2} \quad (23)$$

where $u \in [0, 1]$ is a uniform random number, and $p(u)$ is the related simulated value of extreme roughness amplitude. In this paper, we shall noticed $p(u) = \hat{Y}_{\max}^{l_0, k}$, where l_0 is the length from which extreme roughness is measured and modeled by the Lambda distribution, and k is a coefficient introduced to predict the extreme roughness amplitude at the larger evaluation length $l_0 \times k$. To illustrate this method, this Monte-Carlo procedure is applied to predict the PDF of $\hat{Y}_{\max}^{60 \mu\text{m}, k}$ and $\hat{Y}_{\min}^{60 \mu\text{m}, k}$ for $k \in \{1, 2, 5, 10, 20, 30\}$. Fig. 11 represents these PDF func-

Table 2
Values of the four parameters for the both Lambda distributions that modeled $Y_{\max}^x(60 \mu\text{m})$ and $Y_{\min}^x(60 \mu\text{m})$

	λ_1	λ_2	λ_3	λ_4
$Y_{\max}^x(60 \mu\text{m})$	0.0233	-2.32	-0.010	-0.018
$Y_{\min}^x(60 \mu\text{m})$	0.0199	25.51	0.134	0.199

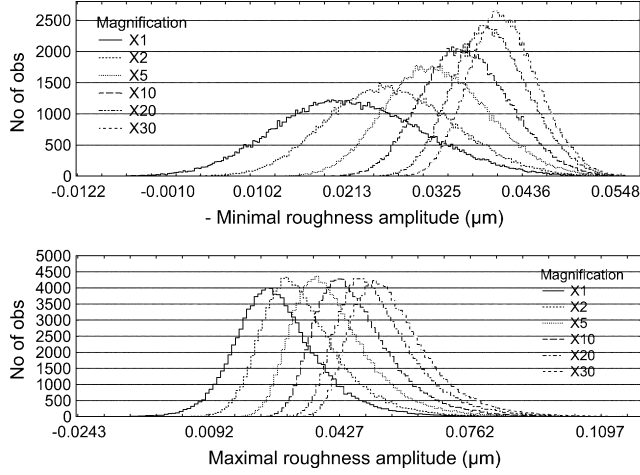


Fig. 11. $\hat{Y}_{\max}^{60\mu\text{m},k}$ (top) and $\hat{Y}_{\min}^{60\mu\text{m},k}$ (bottom) PDF's functions prediction obtained from 10000 Monte-Carlo simulations for the 6 magnifications $k \in \{1,2,5,10,20,30\}$. The case $k=1$ corresponds to simulation of the original Lambda shown on Fig. 10.

tions obtained from 10000 Monte-Carlo simulations. As it can be observed, the mean of the PDF increases as the magnification k increases. From these empirical probability density functions, usual statistical estimators like the mean and the 90% confidence interval (i.e., the difference between the 95th and the 5th percentiles) can then be easily determined to assess respectively, the central tendency and the dispersion. Since one problem of practical importance is to determine the extreme roughness amplitude that will be found in a large scale sample by using a small evaluation length, the procedure was used again to assess the effect of the surface size on the evolution of the mean and the 90% confidence interval of the distribution of the extreme values of amplitude. Fig. 12 shows the mean of the maximum extreme roughness amplitude versus the evaluation length. Analyzing the roughness at a $60\mu\text{m}$ evaluation length, allows predicting the roughness at all the scales larger than $2000\mu\text{m}$ and moreover the 90% confidence interval also seems to be a good model since the nine experimental curves are scattered in this interval. Note that like experimental curves, confidence interval increases with the evaluation length or more precisely when the prediction is model farther from the scale at which Lambda distribution is computed (i.e., from which our predictive model is constructed). However, when the maximal range amplitude $\hat{R}_t^{60\mu\text{m},k}$ is computed (Fig. 13) with the same procedure as described above, a high inaccuracy appears in our modelling and $\hat{R}_t^{60\mu\text{m},k}$ minimizes the real Peak to Valley parameter amplitude. We shall briefly explain this fact: the simulation supposes that predicting a two-fold length amplitude value is equivalent to choosing two values in the initial density and taking the maximal one. However, this reasoning does not hold for $\hat{R}_t^{60\mu\text{m},k}$ because the minimal value and the maximal value are not computed at the same scale. Let us illustrate this purpose by a simple example without lack of generality. Considering the profile given on Fig. 14, at the larger scale $l=7000$, $Y_{\max}^0(l) = 1$, $Y_{\min}^0(l) = 0$ and then $R_t^0(l) = Y_{\max}^0(l) - Y_{\min}^0(l) = 1$ (this relation will always hold whatever the profile into consideration).

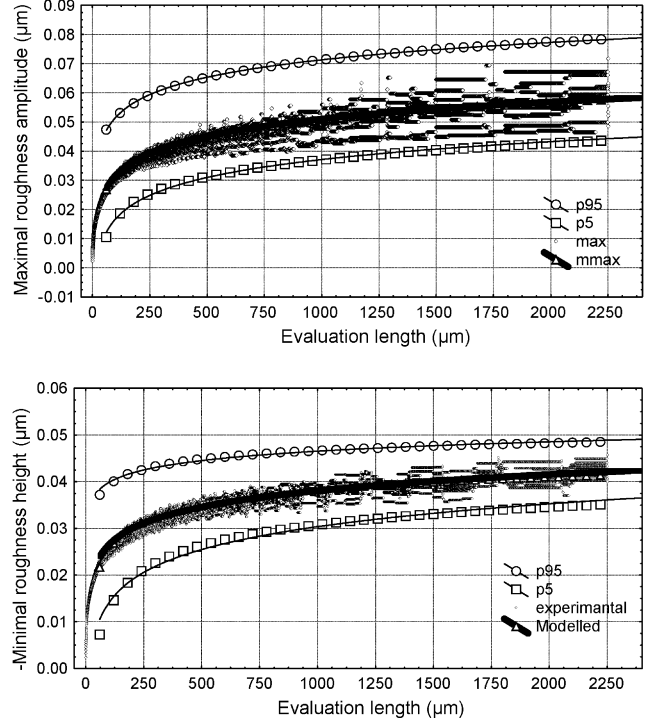


Fig. 12. Prevision of the mean of the extreme roughness amplitude parameters $\hat{Y}_{\max}^{60\mu\text{m},k}$, $\hat{Y}_{\min}^{60\mu\text{m},k}$ (\blacktriangle) vs. the evaluation length (obtained by taking all k values) and their associated 5th (\circ) and 95th (\square) quantile confidence intervals. The 9 experimental curves are plotted (\diamond).

At scale $l/2$, one gets $R_t^0(l/2) = 0.1$, $R_t^{3500}(l/2) = 0.1$ and $R_t^0(l) > \max(R_t^0(l/2), R_t^{3500}(l/2)) = 0.1$. However, one always gets $Y_{\max}^0(l) = \max(Y_{\max}^0(l/2), Y_{\max}^{3500}(l/2)) = 1$ and $Y_{\min}^0(l) = \min(Y_{\min}^0(l/2), Y_{\min}^{3500}(l/2)) = 0$. This clearly means the well-known ‘‘Peak to Valley’’ is not an extreme value parameter. To predict its value, it is possible to use the extreme value theory on the minimal and maximal amplitude thanks to the general relation.

$$\hat{R}_{t2}^{60\mu\text{m},k} = \hat{Y}_{\max}^{60\mu\text{m},k} - \hat{Y}_{\min}^{60\mu\text{m},k} \quad (24)$$

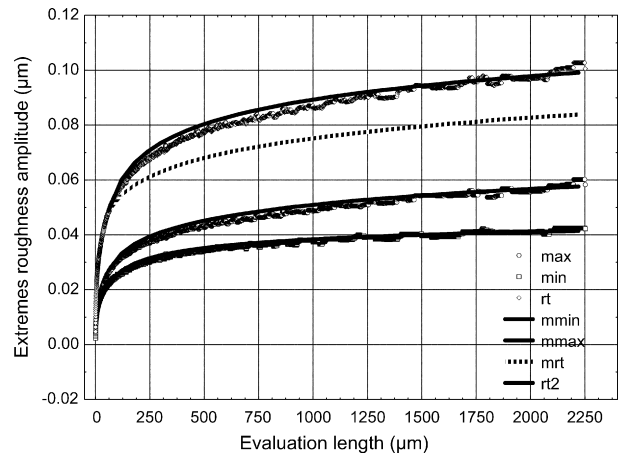


Fig. 13. Mean of the extreme roughness amplitude parameters $\hat{Y}_{\max}^{60\mu\text{m},k}$, $\hat{Y}_{\min}^{60\mu\text{m},k}$, $\hat{R}_t^{60\mu\text{m},k}$ and $\hat{R}_{t2}^{60\mu\text{m},k} = \hat{Y}_{\max}^{60\mu\text{m},k} - \hat{Y}_{\min}^{60\mu\text{m},k}$ (lines) prevision vs. the evaluation length and the $Y_{\max}(l)$, $Y_{\min}(l)$ and $R_t(l)$ means experimental values.

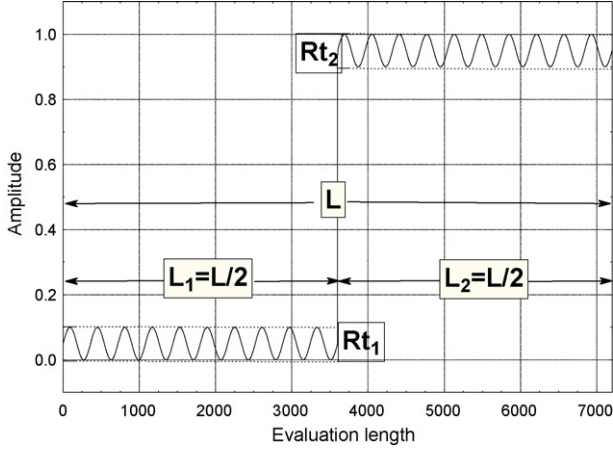


Fig. 14. Combination of a heavy side function with a sinusoid.

which gives the probability density function of the Peak to Valley roughness parameters. As it can be observed on Fig. 13, the Peak to Valley amplitude is well modeled from $60 \mu\text{m}$ until more than $2000 \mu\text{m}$. The relation Eq. (24) will be essential in many fields where the “Peak to Valley” parameter is of major interest (geometrical tolerance, fluid mechanics, wear. . .).

In the preceding case, the prevision of maximal roughness parameters was calculated by taking at origin the sampling length $l=60 \mu\text{m}$ (end of the fractal stage). Now, the same result will be computed by taking the origin in the

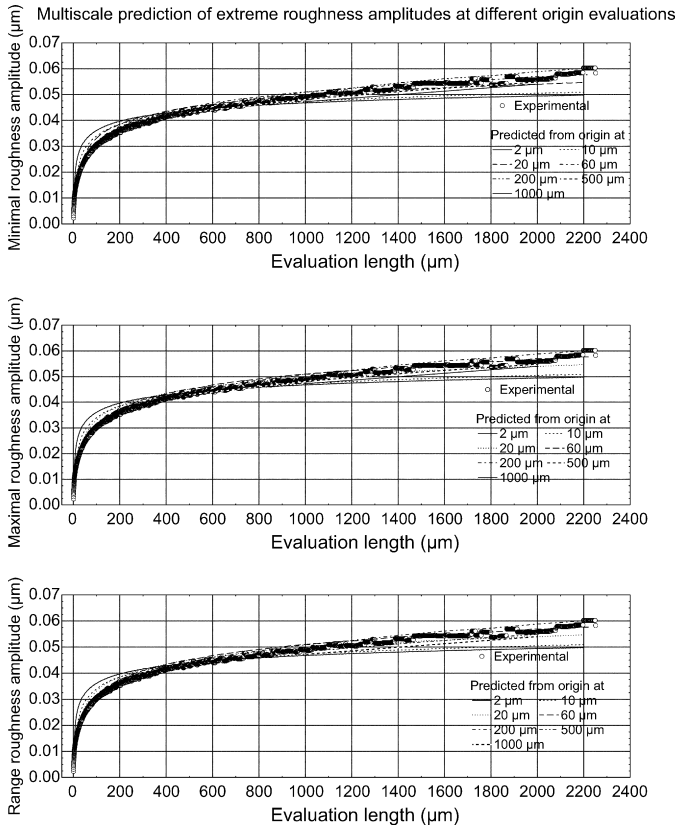


Fig. 15. Multi-scale prediction of extreme roughness amplitudes parameters $\hat{Y}_{\min}^{x,k}$, $\hat{Y}_{\max}^{x,k}$, $\hat{R}_t^{x,k}$ at different origin evaluations $x \in \{2, 10, 20, 60, 200, 500, 1000\}$.

Stage I, Stage II and another origin points in the Stage III ($l \in \{2, 10, 20, 60, 200, 500, 1000\} \mu\text{m}$). Fig. 15 shows the evolution of the maximal roughness amplitude parameters predicted for these different origins. For all the parameters under study, the prediction always holds with a very good accuracy for $l > 60 \mu\text{m}$. This confirms that stage III, as opposed to stages I and II, is an extreme value stage as claimed in the preceding chapters and validates our methodology at all the scale.

5. Conclusion

This paper is a contribution to estimate the control tolerance in the field of high precision machined surfaces that can be generalized to other physical or mechanical processes. The micromachined workpieces may first be modeled by fractal functions and we provide an analytical modelling of the surface topography. The multi-scale analysis performed in this paper shows that roughness recorded by mechanical profilometer from high precision turning surfaces present three behaviors. A smoothing effect related to the recording apparatus tip radius of curvature (stage I), a fractal range (stage II) characterized by the fractal dimension and a stage III characterized by the Extreme values theory. This last stage is modeled by a new and alternative methodology to the Gumbel approach combining the Generalized Lambda Distribution and the Monte-Carlo method in order to estimate accurately the maximal peaks and minimal valleys. Finally, a method is proposed to predict the mean with a 90% confidence interval of the maximal valleys, minimum peaks and the “Peak to Valley” roughness parameters by measuring a roughness profiles at a lower scale. In a future works, this methodology will be applied to predict the value of others roughness parameters like R_a , R_q . . . known to be relevant to influence a physical response on the surface.

Appendix A. Annexe

This part aims to create a new fractal function that describes the turning process. We shall assume that the part of the diamond tool in contact with the aluminium workpiece has approximately, a hemispherical shape and then the grooves can be seen as indentations having a circular shape, which follows a power law. As a consequence, the profile is described as a sum of elementary half-circles. Let us first define an elementary function $g(x)$ of period 1 on the $[0..1]$ interval as follows:

$$g(x) = -1 - (x - 0.5)^2 \quad x \in [0, 1] \quad (\text{A.1})$$

We then propose the deterministic fractal circle function:

$$F_{CF}(x) = A \sum_{n=0}^{\infty} 2^{-nH} g(2^n x) \quad (\text{A.2})$$

where $H \in [0..1]$ and A is a scaling amplitude factor.

Theorem: the fractal dimension of the profile $\Delta(G_f)$ is given by:

$$\Delta(G_f) = 2 - H \quad (\text{A.3})$$

To take into account the stochastic component of experimental profiles, a stochastic version of the previous function given by Eq. (a2) must be formulated:

$$F_{\text{SCF}}(x) = A \prod_{n=0}^{\infty} \Psi_n 2^{-nH} g(2^n x + \varphi_n) \quad (\text{A.4})$$

where Ψ_n are positive Gaussian random numbers that physically represent the stochastic variation of the stress during the turning process, and φ_n are uniform random numbers that represent the disorientation of the grooves due to the rotation of the turning tool. These numbers leave the fractal dimension unchanged. Only a few terms are needed to discretize the curve because of the exponential decrease of the period in the $g(x)$ function. For $n=0$ the function is defined on $[0..1]$, $n=1$ on $[0..0.5]$, $n=2$ on $[0..0.25]$ and so on. This means that very quickly the period of the function will reach the sampling length. Consequently the shape of elementary functions will often appear on the graph of $F_{\text{SCF}}(x)$. To avoid this numerical artefact, we have to add new terms to the fractal series without modifying the fractal dimension. We then retain the new function:

$$F_{\text{MSCF}}(x) = A \prod_{n=0}^{\infty} \Psi_n 2^{-nH/p} g(2^{n/p} x + \varphi_n) \quad (\text{A.5})$$

with p an integer higher than unity.

As a consequence, the spectrum of the function related to Eq. (a5) tends to be more continuous than those described in the bibliography. It can be noticed that only two parameters have to be determined for the definition of the Fractal Circle Function proposed in this paper: the amplitude factor A and the Hölder exponents H . The p value is chosen to be high enough ($p=10$) so as to avoid statistical artefacts in the spectrum representation. H is given by the slope on stage II of the curves shown in Fig. 3. A is calculated such simulated profiles and experimental ones lead to the same R_a value (average roughness amplitude).

References

- [1] A. Goyal, V. Hood, S. Tadigadapa, High speed anisotropic etching of Pyrex® for microsystems applications, *J. Non-Crystalline Solids* 352 (6–7) (2006) 657–663.
- [2] K. Biswas, S. Kal, Etch characteristics of KOH, TMAH and dual doped TMAH for bulk micromachining of silicon, *Microelectron. J.* 37 (6) (2006) 519–525.
- [3] K. Honer, G. Kovacs, Integration of sputtered silicon microstructures with pre-fabricated CMOS circuitry, *Sens. Actuators A* 91 (3) (2001) 386–397.
- [4] M. Föhse, T. Kohlmeier, H.H. Gatzert, Thin film technologies to fabricate a linear microactuator, *Sens. Actuators A* 91 (1–2) (2001) 145–149.
- [5] H.S. Liu, B. Yan, F. Huang, K. Qiu, A study on the characterization of high nickel alloy micro-holes using micro-EDM and their applications, *J. Mat. Proc. Tech.* 169 (3) (2005) 418–426.
- [6] C. Lin, F. Tseng, A micro Fabry-Perot sensor for nano-lateral displacement sensing with enhanced sensitivity and pressure resistance, *Sens. Actuators A Phys.* 114 (2–3) (2004) 163–170.
- [7] H. Liu, B. Bhushan, Nanotribological characterization of digital micromirror devices using an atomic force microscope, *Ultramicroscopy* 100 (3–4) (2004) 391–412.
- [8] B. Bhushan, T. Kasai, G. Kulik, L. Barbieri, P. Hoffmann, AFM study of perfluoroalkylsilane and alkylsilane self-assembled monolayers for anti-stiction in MEMS/NEMS, *Ultramicroscopy* 105 (1–4) (2005) 176–188.
- [9] R. Bandorf, H. Lüthje, C. Henke, J.H. Sick, R. Küster, Tribological behaviour of thin a-C and a-C:H films with different topographic structure under rotating and oscillating motion for dry lubrication, *Surf. Coat. Tech.* 188–189 (2004) 530–533.
- [10] S. Chandrasekaran, S. Sundararajan, Effect of microfabrication processes on surface roughness parameters of silicon surfaces, *Surf. Coat. Tech.* 188–189 (2004) 581–587.
- [11] S. Sundararajan, B. Bhushan, Micro/nanotribological studies of polysilicon and SiC films for MEMS applications, *Wear* 217 (2) (1998) 251–261.
- [12] W.M. Zhang, G. Meng, Numerical simulation of sliding wear between the rotor bushing and ground plane in micromotors, *Sens. Actuators A Phys* 126 (1) (2006) 15–24.
- [13] M. Bonis, P. Revel, C. Tirvaudey, J.L. Vavrille, *Journées de l’AUM*, Saint Etienne, 1998.
- [14] C. Evans, *Precision Engineering: An Evolutionary View*, Cranfield Press, Bedford, UK, 1989.
- [15] P. Hannah, R. Rohrer, *Basics of diamond turning*, Tutorial, ASPE, 1990.
- [16] W. König, M. Weck, N. Spenrath, J. Luderich, *Tutorial on Diamond Machining Technology*, 6th IPES/UME 2, Braunschweig, 1991.
- [17] S.C. Fawcett, R.F. Keltie, Use of a fiber optic displacement probe as a surface finish sensor, *Sens. Actuators A Phys.* 24 (1) (1990) 5–14.
- [18] H.W. Zhou, B.G. Kharas, P.I. Gouma, Microstructure of thick polycrystalline silicon films for MEMS application, *Sens. Actuators A Phys.* 104 (1) (2003) 1–5.
- [19] M. Hasegawa, J. Liu, K. Okuda, Calculation of the fractal dimension of machined surface profiles, *Wear* 192 (1996) 40–45.
- [20] B. Dubuc, J.F. Quiniou, C. Roques-Carnes, C. Tricot, S.W. Zucker, Evaluating the fractal dimension of profiles, *Phys. Rev. A* 39 (3) (1989) 1500–1512.
- [21] H. Khanfir, M. Bonis, P. Revel, Improving flatness in ultraprecision machining by attenuating spindle motion errors, *Int. J. Mach. Tools Manuf.* 45 (7–8) (2005) 841–848.
- [22] H. Khanfir, PhD dissertation, Univ. Tech. Compiègne, France, 2002.
- [23] Z.J. Yuan, M. Zhou, S. Dong, Effect of diamond tool sharpness on minimum cutting thickness and cutting surface integrity in ultraprecision machining, *J. Mat. Proc. Tech.* 62 (4) (1996) 327–330.
- [24] J.M. Oomen, J. Eisses, Wear of monocrystalline diamond tools during ultra precision machining of nonferrous metals, *Prec. Eng.* 14 (1992) 206–218.
- [25] R.Y. Fillit, P. Revel, H. Khanfir, M. Bonis, O. Jautzy, Microstructural analysis of ultra precision machined materials., in: *Proceedings of the 2nd EUSPEN Conference*, Bremen, Germany, 1999, pp. 459–462.
- [26] D. Whebi, *Approche fractale de la rugosité des surfaces et implication analytique*, PhD Thesis, Besançon, France, 1986.
- [27] B.B. Mandelbrot, *The Fractal Geometry of Nature*, W.H. Freeman and Company, New York, 1983.
- [28] C. Tricot, *Courbes et dimension fractale*, Springer-Verlag, Paris, 1993.
- [29] M. Biggerelle, A. Iost, Bootstrap analysis of fatigue crack growth rate: application on the Paris’ relationship and to lifetime prediction, *Int. J. Fatigue* 21 (4) (1999) 299–307.
- [30] G. Palasantzas, J.Th.M. DeHosson, Surface roughness influence on the pull-in voltage of microswitches in presence of thermal and quantum vacuum fluctuations, *Surf. Sci.* 600 (7) (2006) 1450–1455.
- [31] C.A. Brown, W.A. Johnsen, R.M. Butland, Scale-sensitive fractal analysis of turned surface, *Ann. CIRP* 45 (1996) 515–518.
- [32] M. Hasegawa, J. Liu, K. Okuda, Calculation of the fractal dimension of machined surface profiles, *Wear* 192 (1996) 40–45.
- [33] M.C. Kang, J.S. Kim, K.H. Kim, Fractal dimension analysis of machined surface depending on coated tool wear, *Surf. Coat. Tech.* 193 (1–3) (2005) 259–265.
- [34] L. Shangping, L. Jie, L. Li, C. Shousheng, S. Wengui, P. Huiqin, Study of the round workpiece surface topography in high-speed precision grinding using a scanning tunneling microscopy, *J. Mat. Proc. Tech.* 139 (1–3) (2003) 263–266.
- [35] Z. Jiang, H. Wang, B. Fei, Research into the application of fractal geometry in characterising machined surfaces, *Int. J. Mach. Tools Manuf.* 41 (13–14) (2001) 2179–2185.
- [36] G. Zhang, S. Gopalakrishnan, Fractal geometry applied to on-line monitoring of surface finish, *Int. J. Mach. Tools Manuf.* 36 (10) (1996) 1137–1150.

- [37] G. Galante, A. Lombardo, M. Piacentini, Fractal dimension: a useful tool to describe the microgeometry of machined surfaces, *Int. J. Mach. Tools Manuf.* 33 (4) (1993) 525–530.
- [38] T.H. Fang, W.J. Chang, Effects of AFM-based nanomachining process on aluminum surface, *J. Phys. Chem. Sol.* 64 (6) (2003) 913–918.
- [39] J. Lopez, G. Hansali, J.C. Le Bossa, T. Mathia, Caractérisation fractale de la rugosité tridimensionnelle d'une surface, *J. Phys. III* 4 (1994) 2501–2519.
- [40] B.B. Mandelbrot, J.W. Van Ness, Fractional Brownian motions, fractional noises and applications, *SIAM Rev.* 10 (1968) 422–437.
- [41] C.Y. Poon, B. Bhusham, Comparison of surface roughness measurements by stylus profiler, AFM, and non-contact optical profiler, *Wear* 190 (1995) 76–88.
- [42] J.I. Mc Cool, Comparison of models for the contact of rough surfaces, *Wear* 107 (1986) 37–60.
- [43] V. Radhakrishnan, Effect of stylus radius on the roughness values measured with tracing stylus instruments, *Wear* 16 (1970) 325–335.
- [44] D.J. Whitehouse, Theoretical analysis of stylus integration, *Ann. CIRP* 23 (1974) 181–182.
- [45] T. Nakamura, On deformation of surface roughness curves caused by finite radius of stylus tip and tilting of stylus holder arm, *Bull. Jpn. Soc. Precision Eng.* 1 (1966) 240–248.
- [46] R. Ohlsson, A. Wihlborg, H. Westberg, The accuracy of fast 3D topography measurements, *Int. J. Mach. Tools Manuf.* 41 (13–14) (2001) 1899–1907.
- [47] S.S. Sheiko, M. Möller, E.M.C.M. Reuvekamp, H.W. Zandbergen, Evaluation of the probing profile of scanning force microscopy tips, *Ultra-microscopy* 53 (4) (1994) 371–380.
- [48] P.E. Mazeran, L. Odoni, J.L. Loubet, Curvature radius analysis for scanning probe microscopy, *Surf. Sci.* 585 (1–2) (2005) 25–37.
- [49] E.J. Gumbel, Statistical theory of extreme values and some practical applications, *Applied Mathematics Series 33*, National Bureau of Standards, Washington DC, 1954.
- [50] Z.A. Karian, E.J. Dudewicz, Fitting Statistical Distributions, The Generalized Lambda Distribution and Generalized Bootstrap Methods, Chapman & Hall, CRC Press, Boca Raton, Florida, 2000.

Biographies

Maxence Bigerelle, Professor in Materials Science, Engineer in Computer Sciences, Ph.D. in Mechanic and Material Sciences (1999), Medical Expert in Biomaterials at the University Hospital Centre of Lille, Capacitation of Research Directorship in Physical Sciences (2002). Field of Interests: Surfaces and Interfaces morphological characterisation, Multi-scale Modelling, Fractal & Chaos, Biomaterials and Nanostructures. Actually, Director Assistant of the Materials Research Group in the Laboratory Roberval, FRE 2833, UTC/CNRS, Centre de Recherches de Royallieu, BP20529, 60205 Compiègne France.

Alexis Gautier, Ph.D. Student, Engineer in Mechanic, Field of Interests: tool machining process, Micro-Machining, Optical Properties of MEMS, Metrology. Laboratory Roberval, FRE 2833, UTC/CNRS, Centre de Recherches de Royallieu, BP20529, 60205 Compiègne France.

Alain Iost, is Professor of Metallurgy and Materials Science at “ENSAM Lille” and leader of the team “Characterisation and Properties of Perisurfaces” at the Physical Metallurgy and Material Engineering Laboratory. The main fields of interest are the mechanical and morphological characterization of Surfaces and Interfaces.